



# Multifunctional 2.5D metastructures enabled by adjoint optimization

MAHDAD MANSOOREE,<sup>1,†</sup> HYOUNGHAN KWON,<sup>2,†</sup> EHSAN ARBABI,<sup>2</sup> ANDREW McCLUNG,<sup>1</sup>   
ANDREI FARAON,<sup>2</sup>  AND AMIR ARBABI<sup>1,\*</sup> 

<sup>1</sup>Department of Electrical and Computer Engineering, University of Massachusetts Amherst, 151 Holdsworth Way, Amherst, Massachusetts 01003, USA

<sup>2</sup>T. J. Watson Laboratory of Applied Physics and Kavli Nanoscience Institute, California Institute of Technology, 1200 East California Boulevard, Pasadena, California 91125, USA

\*Corresponding author: arbabi@umass.edu

Received 6 August 2019; revised 2 December 2019; accepted 10 December 2019 (Doc. ID 374787); published 17 January 2020

Optical metasurfaces are two-dimensional arrays of meta-atoms that modify different characteristics of light such as phase, amplitude, and polarization. One intriguing feature that distinguishes them from conventional optical components is their multifunctional capability. However, multifunctional metasurfaces with efficiencies approaching those of their single-functional counterparts require more degrees of freedom. Here we show that 2.5D metastructures, which are stacked layers of interacting metasurface layers, provide sufficient degrees of freedom to implement efficient multifunctional devices. The large number of design parameters and their intricate intercoupling make the design of multifunctional 2.5D metastructures a complex task, and unit-cell approaches to metasurface design produce suboptimal devices. We address this issue by designing 2.5D metastructures using the adjoint optimization technique. Instead of designing unit cells individually, our technique considers the structure as a whole, accurately accounting for interpost and inter-layer coupling. As proof of concept, we experimentally demonstrate a double-wavelength metastructure, designed using adjoint optimization, that has significantly higher efficiencies than a similar device designed with a simplified approach conventionally used in metasurface design. The 2.5D metastructure architecture empowered by the optimization-based design technique is a general platform for realizing high-performance multifunctional components and systems. © 2020 Optical Society of America under the terms of the [OSA Open Access Publishing Agreement](#)

<https://doi.org/10.1364/OPTICA.374787>

## 1. INTRODUCTION

Metasurfaces, a new class of diffractive optical elements engineered at the subwavelength, have recently emerged as a promising platform for compact optical elements with enhanced and augmented functionalities [1–10]. They have garnered great interest due to their versatility, ease of fabrication, and their multifunctional capability. Various metasurface-based devices and systems such as lenses [6,11,12], beam splitters [7,13], polarization elements [7,14], and flat spectrometers and retroreflectors [15,16] have been demonstrated. One of the main features that distinguishes metasurfaces from conventional optical components is their multifunctional capability. A multifunctional metasurface performs different functions based on different characteristics of an incident wave such as polarization [7,14,17], wavelength [9,18–22], and incidence angle [23]. Implementation of multifunctional metasurfaces requires independent control of optical wavefronts for different degrees of freedom of the incident wave [5,9,18–22,24]. To design multifunctional metasurfaces, a few different methods have so far been investigated, including spatial multiplexing [5,22,24] using multi-element unit cells [9,19,21] or meta-atoms

with additional degrees of freedom [20,21]. However, these methods have both fundamental and practical shortcomings as they do not generally provide sufficiently many degrees of freedom to achieve multifunctional response [5,9,19,21,22,25], resulting in devices with lower efficiencies that are less tolerant to fabrication errors.

Multilayer metasurfaces provide a significantly larger number of degrees of freedom and can be used for the implementation of multifunctional devices. Reference [18] recently demonstrated multiwavelength bilayer metasurfaces assuming layers to be non-interacting. However, considering interlayer interactions (evanescent coupling or unwanted diffracted propagating fields) allows one to leverage even more degrees of freedom for similarly-sized metasurfaces, promising higher-performing devices. Highly coupled multilayer metasurfaces can be considered as 2.5D aperiodic metamaterials [Fig. 1(a)]. Metamaterials and photonic crystals are periodic 3D arrangements of meta-atoms designed to achieve desired effective material properties or band structures, and are fully described by one of their unit cells. By contrast, 2.5D metastructures are composed of dissimilar interacting meta-atoms with a large number of design parameters. The methods that are

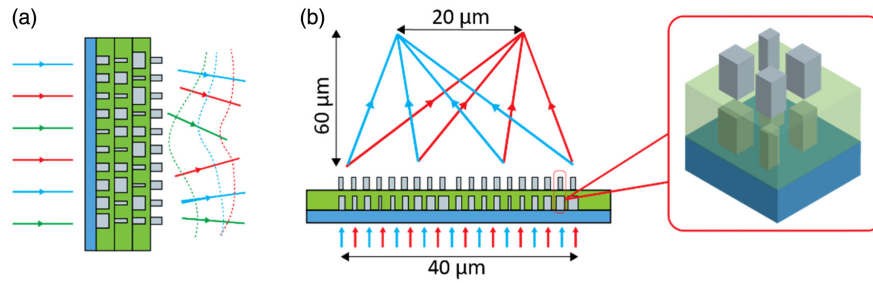


**Fig. 1.** Multifunctional 2.5D metastructure. (a) Schematic of a metastructure with the ability to generate independent wavefronts for different wavelengths. (b) Illustration of one such metastructure which focuses two different wavelengths to two separate focal points. The inset shows a closer picture of a part of the device.

conventionally used to design single-layer metasurfaces are not accurate for designing 2.5D devices due to multiple reflections and diffraction of light between the layers that lead to nonlocal interactions among meta-atoms in different layers. To address this issue, here we develop and use an adjoint optimization technique to design 2.5D metastructures.

Adjoint optimization [26–30] is a versatile and powerful technique that has been used in the electromagnetics and optics communities to design various devices such as couplers and beam splitters [31], integrated components [32–35], and photonic crystals [26]. It has also been utilized to design single-layer [36–38] and multi-layer [39–41] metasurfaces; however, its applications have been mostly limited to periodic structures [36,42] or 2D metasurfaces, resulting in a simpler formulation and implementation.

Here, we experimentally demonstrate 2.5D multifunctional metastructures designed using adjoint optimization. In contrast to most demonstrations so far that use a topological optimization scheme, we use parameterized meta-atoms that are more suitable for the layer-by-layer fabrication. For performance comparison, we designed a control device using a direct design technique that ignores the diffraction and scattering of light in the regions between the stacked layers that cause the non-locality of the interactions. The simulated and experimentally measured focusing efficiencies of the optimized device were found to be significantly higher than the simulated efficiency of the control, confirming the potential of the adjoint-based technique in designing high-performance 2.5D multifunctional devices. In the following, we discuss a direct design strategy for implementing 2.5D metastructures and study its performance via full-wave simulations, and then we describe the adjoint-based design approach.

## 2. DIRECT DESIGN

The direct design method uses maps that relate the optical response of a unit cell to geometrical parameters of meta-atoms within it. Metastructures designed with this method use these maps to determine the spatial arrangement of dissimilar unit cells that implement the desired optical transformation. In the direct design paradigm, the multifunctional 2.5D metastructure shown in Fig. 1(a) can be conceptualized as a 2D array of unit cells in which each unit cell consists of stacked meta-atoms.

An underlying assumption in direct design is that the transmission amplitude of a unit cell in an aperiodic metasurface can be approximated by the transmission amplitude of the same unit cell in a periodic metasurface. The approximation is valid when the

meta-atom geometries vary slowly and the metasurface is nearly periodic in the vicinity of each meta-atom. However, the accuracy of the approximation decreases as the interactions between neighboring unit cells deviate from those of a periodic structure. In design of multilayer metasurfaces with conventional direct design, the deviation of the meta-atoms from perfect periodicity in one layer leads to scattering and diffraction of the waves in the spacer layers and non-local excitation of the meta-atoms in the following layers. As a result, the accuracy of the direct technique for modeling and designing multilayer metasurfaces decreases as the number of layers increases.

To illustrate its shortcomings, we use the direct design method to design and evaluate the performance of a lens that focuses light to two separate focal spots based on its wavelength [Fig. 1(b)]. The bilayer structure is composed of more than 21,000 amorphous silicon meta-atoms arranged in two stacked layers. The bilayer meta-atoms are nano-posts with square cross-sections, and are placed on a periodic square lattice. The device has a diameter of 40 μm and focuses  $\lambda_1 = 780$  nm and  $\lambda_2 = 915$  nm light to two points 60 μm away from it. These two wavelengths were selected because of the availability of sources at these wavelengths.

The unit cell of the bilayer metastructure is schematically shown in Fig. 2(a), denoting the dimensions. Assume that the structure is illuminated by two normally incident plane waves with wavelengths of  $\lambda_1$  and  $\lambda_2$ . The transmission phases at the two wavelengths ( $\phi_1$  and  $\phi_2$ ) depend on many design parameters (layer height, interlayer distance, and material indices, to name just a few). We select as design parameters the nano-post widths  $W_b$  and  $W_t$  of the top and bottom layers, respectively. In the direct design paradigm, it is assumed that complete and independent control of  $\phi_1$  and  $\phi_2$  can be achieved by tuning these widths. To generate the direct design maps shown in Fig. 2(b), we found the transmission coefficients ( $t_1$  and  $t_2$ ) of the periodic bilayer metastructure shown in Fig. 2(a) as functions of  $W_b$  and  $W_t$  using the rigorous coupled-wave analysis technique [43]. Then, for any combinations of desired phase shifts  $\phi_1$  and  $\phi_2$ , we found optimal values for the nano-post widths  $W_b$  and  $W_t$  such that the transmission coefficients of the periodic bilayer metastructure were closest to  $e^{-j\phi_1}$  and  $e^{-j\phi_2}$  at  $\lambda_1$ , and  $\lambda_2$ , respectively (see Supplementary Fig. S1). The optimal nano-post widths as functions of desired phases are presented in Fig. 2(b). Using the design maps in Fig. 2(b), we designed a double-wavelength bilayer control metalens shown in Fig. 1(b). The metalens imparts spatially varying phase profiles  $\Phi_1 = \frac{2\pi}{\lambda_1} \sqrt{x^2 + (y + \frac{d}{2})^2} + f^2$  and  $\Phi_2 = \frac{2\pi}{\lambda_2} \sqrt{x^2 + (y - \frac{d}{2})^2} + f^2$  at  $\lambda_1$  and  $\lambda_2$ , respectively, where

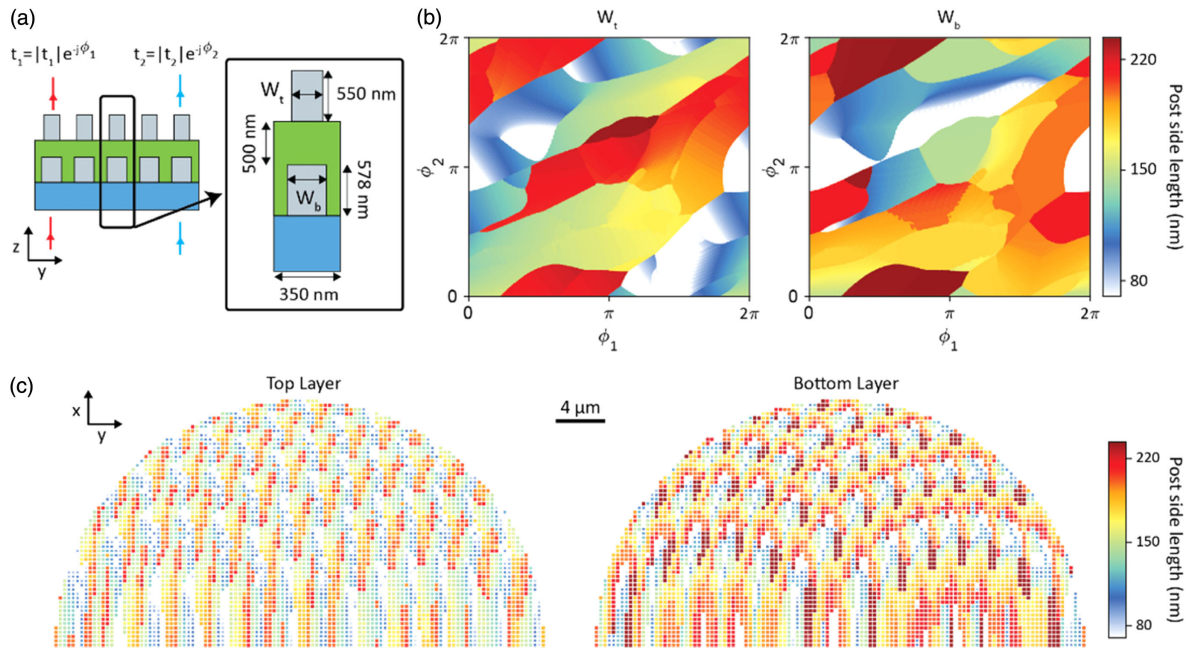


**Fig. 2.** Direct design of metastructures. (a) Illustration of a periodic bilayer metastructure composed of nano-posts with square cross-sections. Transmission coefficients of the metastructure for normally incident light at  $\lambda_1 = 780$  and  $\lambda_2 = 915$  nm are  $t_1$  and  $t_2$ , respectively. The inset shows an expanded view of the unit cell and its dimensions. (b) Optimal widths of the bottom and top nano-posts for achieving  $t_1 = e^{-j\phi_1}$  and  $t_2 = e^{-j\phi_2}$  at  $\lambda_1$  and  $\lambda_2$ , respectively. (c) Color-coded plots of the nano-post width in the top and bottom layers for the control metalens designed using the graphs shown in (b). Because the structure is symmetric with respect to the  $y$  axis, only the nano-post width in the top halves of the layers are plotted.

$f = 60 \mu\text{m}$  is the focal length of the metalens, and  $d = 20 \mu\text{m}$  is the separation between the two focal points. Color-coded width maps of the nano-posts of the bottom and top layers for this device are shown in Fig. 2(c). We refer to this metalens as the control metalens.

The focusing efficiency, defined as the percentage of the incident power focused to a  $3.6 \mu\text{m}$  diameter circle centered at the focal point corresponding to the incident wavelength, was used as a quantitative measure of the device performance. The aperture diameter was selected as  $3.6 \mu\text{m}$  to match the diameter of the aperture used in the measurements discussed below (see Section 4). The focusing efficiencies of the control metalens estimated by the direct design method are 86% and 88% at  $\lambda_1$  and  $\lambda_2$ , respectively. To determine these focal efficiencies more accurately, we performed full-wave simulations in which the device was illuminated by normally incident plane waves with wavelengths  $\lambda_1$  and  $\lambda_2$  (see Supplement 1 for details) [44]. The full-wave simulations yielded focusing efficiencies of 33% and 29%, significantly lower than those predicted by the direct design model. This large discrepancy indicates that the control metalens violates the assumptions of the direct design model, resulting in imperfect implementation of the phase profiles.

### 3. 2.5D METASTRUCTURE DESIGN USING ADJOINT OPTIMIZATION

Because of the inaccuracy of the underlying approximations of the direct design method, high-performance 2.5D metastructures cannot be designed using this method, and a new approach is required that accurately considers the complex interactions between meta-atoms. Here, we employ the adjoint optimization technique to design such metastructures [30,31,36–38,45,46].

In this technique, the desired multifunctional responses of the device are expressed in the form of an objective function, and the design process is cast as an optimization problem. For structures composed of parametrized meta-atoms, the design parameters are the geometrical dimensions of the meta-atoms, and the objective function may be defined as a function of the efficiencies of different functions provided by the device. The meta-atom parameters and the optimal design are determined by maximizing or minimizing the objective function.

In general, the objective function is a nonlinear function of design parameters and the optimization problem is solved iteratively. One approach for solving such a problem is through the gradient descent (or ascent) approach. This approach requires the knowledge of the gradient of the objective function with respect to the design parameters at each iteration, and can be effective provided the gradient vector can be obtained at a reasonable computational cost. The adjoint technique offers an efficient method for the computation of the gradient vector using only two full-wave simulations, namely the forward and adjoint simulations. In the following, we describe the overall design procedure using a bilayer metalens [Fig. 1(b)] as an example.

The design starts by defining an objective function and selecting an initial design. Then, the device is optimized through an iterative procedure. Each iteration consists of two general steps: First, forward and adjoint simulations of the whole structure are performed. The results of these simulations are used to compute the gradient of the objective function with respect to the nano-post widths (see Supplement 1). Second, the nano-post dimensions are updated in small increments using the calculated gradient information. The iterations are continued until no further significant improvement to the objective function is observed.

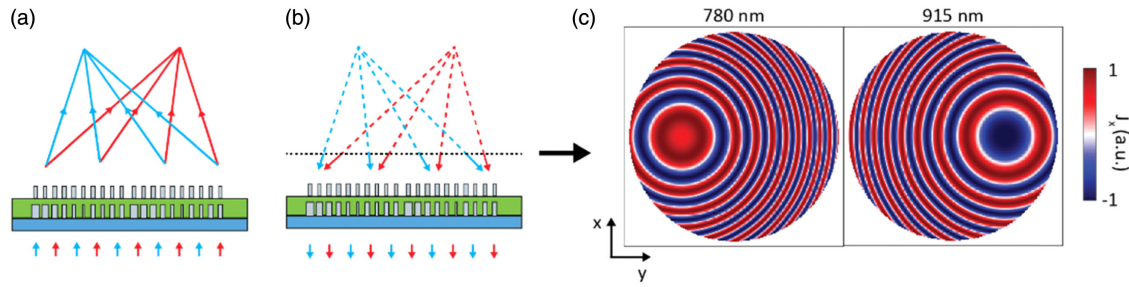


**Fig. 3.** Multiwavelength metalens design using adjoint technique. (a) Schematic representation of the forward, and (b) the adjoint simulations in the adjoint optimization technique. In the forward simulation, the metalens is excited with the incident wave intended for the device operation, while in the adjoint simulation, it is excited by sources that are equal to the time-reversed (i.e., complex conjugate) of the desired output fields. (c) Color-coded plots of the surface electric current densities that are used as excitation sources in the adjoint simulation at the two wavelengths. The current densities are applied on the dotted plane shown in (b).

For the bilayer double-wavelength metalens [Fig. 3(a)], the desired performance metrics are the focal spot intensities for the two wavelengths ( $I_1$  and  $I_2$ ). One possible objective function is the sum of the intensities. However, the optimal solution obtained by

maximizing such an objective function might have significantly different values for  $I_1$  and  $I_2$ . In order to obtain an optimal design with almost equal values for the two intensities, we selected the objective function as  $O = I_1 I_2$ .

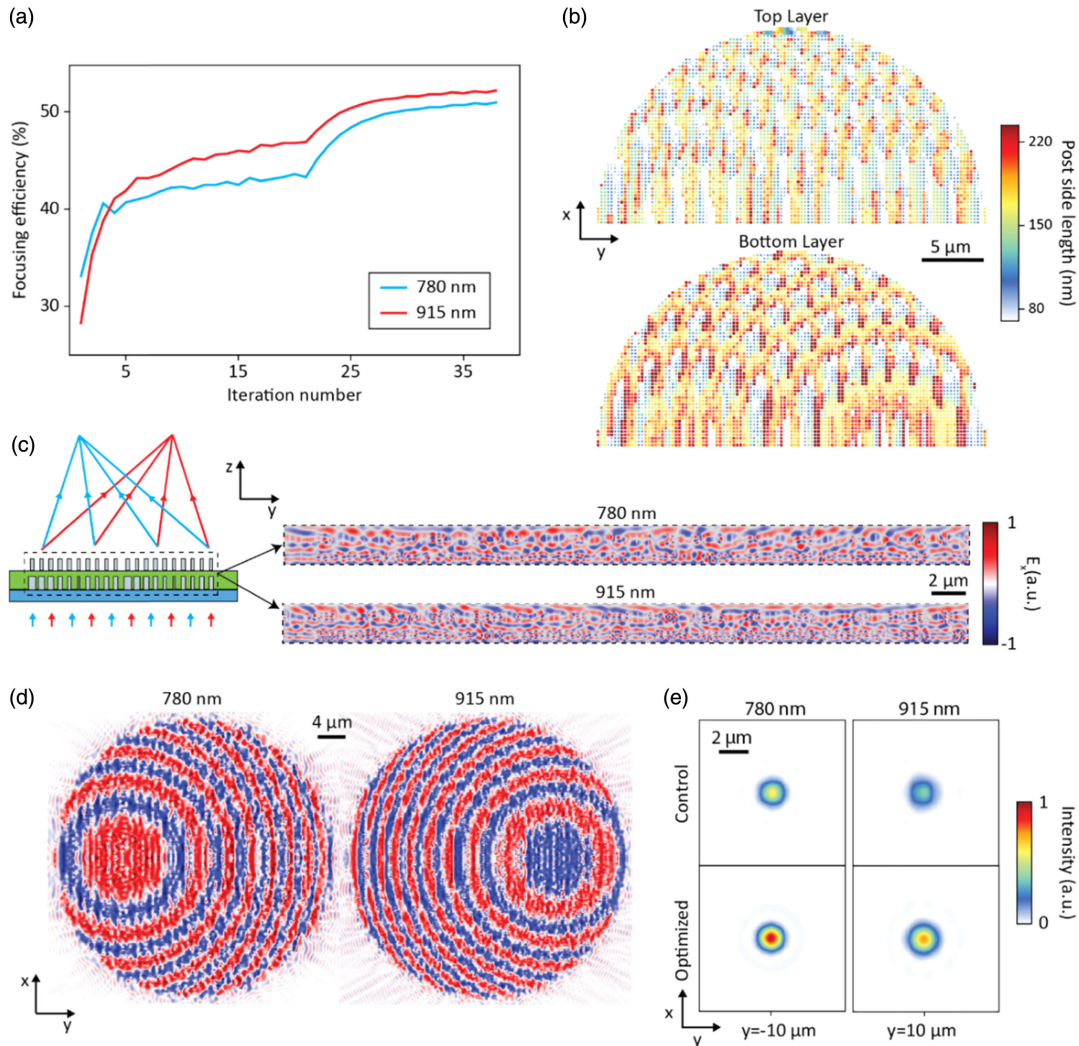


**Fig. 4.** Multifunctional metalens designed using adjoint optimization. (a) Evolution of the focusing efficiencies of the device during the optimization process. (b) Color-coded plots of the nano-post widths in the top and bottom layers for the optimized metalens. Because the structure is symmetric with respect to the  $y$  axis, only the nano-post widths in the top halves of the layers are plotted. (c) Electric field in the  $y-z$  plane in the region indicated by a dashed rectangle in the schematic illustration. (d) Electric field distribution on a plane 78 nm above the optimized metalens at 780 and 915 nm. (e) Simulated intensity distributions in the focal plane of the control and optimized metalenses at 780 and 915 nm.

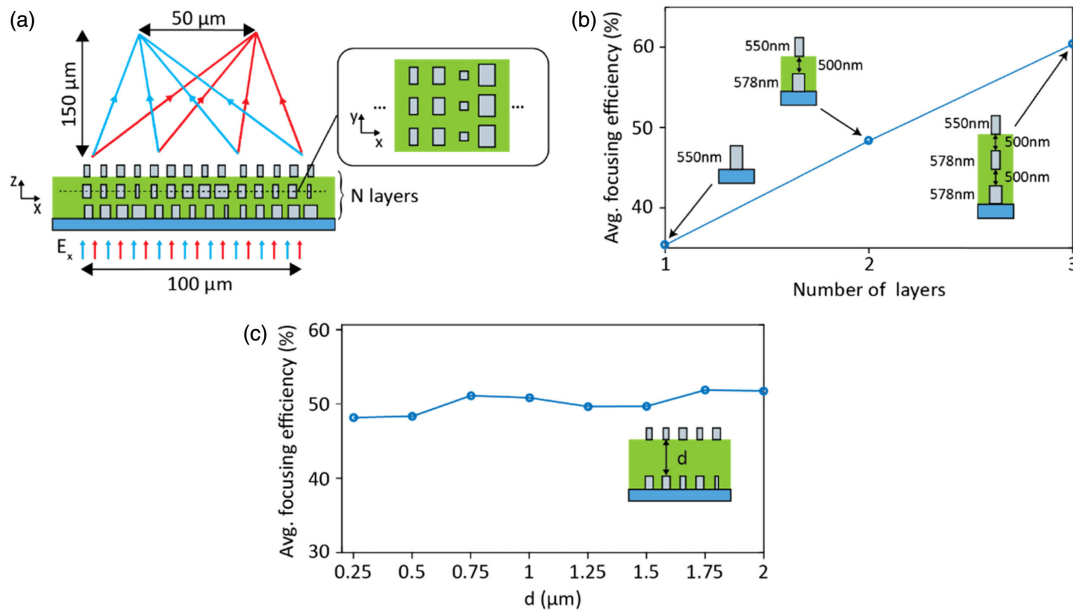


**Fig. 5.** Effects of layer number and interlayer distance. (a) Schematic illustration of a cylindrical multilayer metasurface. The inset shows a cross-section of one layer. (b) Average efficiency (of 780 and 915 nm) for metasurfaces with different numbers of layers, and (c) for bilayer metasurfaces with different spacer thicknesses. Each circle in (a) and (c) shows the final efficiency for different designs.

The gradient of  $O$  with respect to the design parameters was computed using forward and adjoint simulation results (see Supplement 1). Both forward and adjoint simulations are performed using a free and open-source FDTD solver [44], but any electromagnetic field solver (e.g., FDFD, FEM) could be used. In the forward simulation, the metalens is illuminated by incident waves that are used in the device operation. For the double-wavelength metalens, these correspond to normally incident plane waves (i.e., collimated beams) illuminating the metalens aperture [Fig. 3(a)]. In the adjoint simulation, the same structure is excited by sources that are equal to the complex conjugate of the desired output fields (i.e., we propagate the desired output backward). The desired output fields at the two wavelengths are converging spherical waves centered at the corresponding focal points; therefore, the adjoint sources illuminate the metalens by diverging spherical waves centered at the same focal points. This is schematically shown in Fig. 3(b), and a snapshot of the surface current densities that generate such illuminations are shown in Fig. 3(c).

Using this method, we designed the metalens shown in Fig. 1(b) by using the control metalens as the initial design. Figure 4(a) shows the evolution of the focusing efficiencies of the device, which are proportional to  $I_1$  and  $I_2$ , during the optimization process. The optimized device has simulated focusing efficiencies of 52% and 49% at 780 and 915 nm, respectively, for  $x$ -polarized incident light. Color-coded nano-post width maps for the two layers of the optimized metalens are shown in Fig. 4(b). Snapshots of electric field distributions in the  $y-z$  plane are plotted in Fig. 4(c). As Fig. 4(c) shows, the interlayer coupling is significantly more complicated than a simple concatenation of two nano-posts. These interactions contribute to unwanted diffraction, which reduces the performance of designs produced by the direct design method. Snapshots of electric fields in a plane  $\sim 80$  nm above the optimized metalens' top surface are presented in Fig. 4(d). Figure 4(e) shows the focal plane intensities of the control and optimized metalenses.

Both devices are simulated with the same incident waves, and thus the focal spot intensities can be directly compared.

Including additional degrees of freedom in the optimization (e.g., interlayer distance, post layer heights, additional layers of posts) can further increase the device efficiency. To illustrate the effect of adding or removing layers, we compared simulated efficiencies of metasurfaces with one, two, and three layers designed using the adjoint technique (Fig. 5). In this study, we used cylindrical metalenses instead of circular-aperture (“spherical”) metalenses. Cylindrical lenses consist of repeated rows of rectangular meta-atoms, as shown in the inset of Fig. 5(a). Using periodic boundary conditions produces a smaller simulation volume, reducing the computational load and simulation time. The design objective for these cylindrical lenses is analogous to that of the spherical bifocal lens described in the previous section: instead of focusing to two points, the cylindrical lenses focus  $\lambda_1$  and  $\lambda_2$  to two lines, as illustrated in Fig. 5(a). Each lens design starts as a uniform array of meta-atoms with a square cross-section and a width of  $150$  nm.

Figure 5(b) shows the average focusing efficiencies for optimized single-, bi-, and trilayer lenses (see supplementary Fig. S7 for details). The optimized single-layer metasurface has the smallest average efficiency, around 35%. This efficiency increases with the number of layers, to 48% for the bilayer and to 60% for the trilayer lens. These simulations confirm that better performance in multifunctional metasurfaces can be achieved by adding degrees of freedom. As a further demonstration, we also designed larger volume, circular-aperture metalenses with two and three layers that focus  $\lambda_1$  and  $\lambda_2$  to two points on their axes (see Supplement 1). The two focal points were chosen to lie on the metalens axis to reduce the computational cost by exploiting symmetry. In these designs, adding a third layer increased metalens efficiency by  $\sim 15\%$  (Supplement 1, Fig. S3).

We also used cylindrical lenses to study the influence of interlayer distance on device performance. We optimized eight different bilayer metasurfaces with interlayer distance ranging from 250 nm

to  $2\ \mu\text{m}$ . The average efficiency of each device is shown in Fig. 5(c). These results indicate that the performance of the designs obtained using the proposed optimization technique is not highly sensitive to the device parameters. The interlayer distance varies among the designs presented in Fig. 5(c), and their starting design (i.e., the uniform array) differs from the starting design used for the spherical bilayer lens shown in Fig. 4. Despite different parameters and starting designs, both spherical and all cylindrical lenses have reached an average focusing efficiency of  $\sim 50\%$ , thus indicating the relative insensitivity of the optimization-based design approach to different design parameters. The character of nonlocal interactions changes with interlayer distance: evanescent coupling dominates in closely pitched layers, while for more distant layers, diffraction and multiple reflection play larger roles. The performance of the cylindrical lenses is unaffected by interlayer distance

because all these effects are accurately modeled. Though device parameters may be selected arbitrarily, device performance still may be sensitive to deviations from their designed values (i.e., adjoint method designs are not automatically robust). We discuss the impact of inaccurate interlayer distance on device efficiency in Section 4.

#### 4. EXPERIMENTAL RESULTS

We fabricated the 2.5D metalens using standard nano-fabrication techniques. A layer of amorphous silicon was deposited on a fused silica substrate, and the bottom layer meta-atom pattern was generated using electron beam lithography and dry etching. An SU-8 layer was then spin-coated to fill the gaps and cover the first meta-surface, and to act as a spacer between the two layers. The top layer

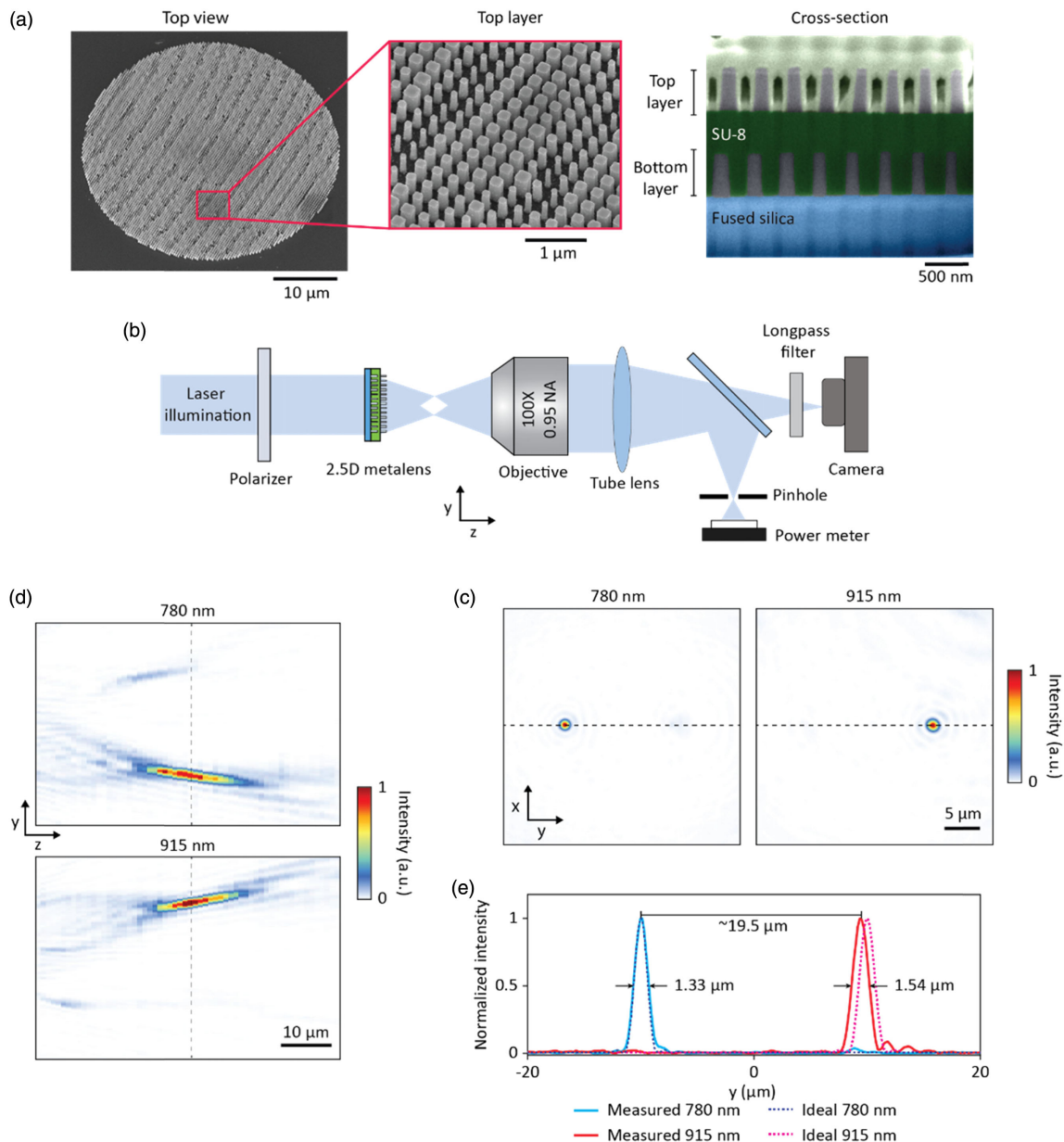


**Fig. 6.** Experimental results. (a) Scanning electron micrographs of the top and cross-sectional view of the 2.5D metalens. A thin, protective platinum layer (light green) was deposited on the top nano-post layer during cross-sectioning. (b) Schematic of the measurement setup used to characterize the bilayer metalens. (c) Intensity distributions measured in the  $y-z$  plane at 780 and 915 nm. (d) Intensity distributions measured in the focal plane of the device at 780 and 915 nm. (e) Intensity profile along the dashed lines shown in (c) and (d) at 780 and 915 nm.

was then fabricated in a process mostly similar to the first one (see Supplement 1 for more details). Scanning electron micrographs of the fabricated devices showing top and cross-sectional views of the device are presented in Fig. 6(a). By repeating the planarization and nano-post fabrication steps, an arbitrary number of layers can be incorporated.

The fabricated metalens was characterized using the setup shown schematically in Fig. 6(b) (see Supplement 1 for more details). Collimated beams from diode lasers at 780 and 915 nm were used to illuminate the device, and the intensity distribution after the device was measured using a custom-built microscope. The intensity distributions captured in the focal plane at both wavelengths are shown in Fig. 6(c) (logarithmic-scale intensity plots are shown in Fig. S4). Figure 5(d) shows the axial intensity distributions (in the  $y-z$  plane) at both wavelengths. As Figs. 5(c) and 5(d) show, the crosstalk between the two focal points is negligible. In Fig. 6(e), the measured full width at half maximum (FWHM) spot sizes are 1.33 and 1.54  $\mu\text{m}$  at 780 and 915 nm, respectively. For comparison, the corresponding FWHMs values for ideal phase profiles are 1.30 and 1.50  $\mu\text{m}$ , respectively, and thus the device shows near-diffraction-limited focusing. To confirm that the device is polarization insensitive, we measured the device with both  $x$ - and  $y$ -polarized input light and observed a negligible polarization dependence (see Fig. S5).

We measured the focusing efficiency of the device at both wavelengths, which is the ratio of optical power focused to a 3.6  $\mu\text{m}$  diameter circle to the power incident on the device, at both wavelengths (see Supplement 1 for details). The measured efficiencies were found to be  $30.3 \pm 0.7\%$  and  $38.2 \pm 1\%$  for  $x$ -polarized light at 780 and 915 nm, respectively and  $33 \pm 1.2\%$  and  $36.5 \pm 1\%$  for  $y$ -polarized light. We attribute the lower measured efficiencies (in comparison to full-wave simulated values of about 50%) to fabrication imperfections, and especially to the difference between the fabricated spacer layer thickness of 800 nm from its designed value of 500 nm. To confirm this, we performed further full-wave simulations of the optimized metalens, but with the actual spacer thickness of 800 nm that resulted in efficiencies of 42% and 38%. Another source of imperfection in 2.5D metasurfaces is misalignment between registered layers. We characterized devices with a relative shift between layers to study this effect (see supplementary Fig. S6 for details). A device with 56 nm shift along the  $x$  axis exhibited a  $-0.8\%$  ( $-4.8\%$ ) change in efficiency for 780 (915) nm light, while a device with the same lateral shift along the  $y$  axis exhibited changes of  $-7.2\%$  ( $+1\%$ ). For reference, the misalignment between layers patterned using electron beam lithography is typically on the order of tens of nanometers.

## 5. DISCUSSION AND CONCLUSION

The versatile 2.5D metastructure platform presented here provides more degrees of freedom than ordinary single layer metasurfaces, enabling the implementation of efficient multifunctional optical devices. By increasing the number of layers or by using more complicated meta-atoms, one can imagine the possibility of integrating additional functionalities by accommodating more wavelengths, different polarizations, or angles of incidence. The conventional direct methods used in designing metasurfaces have a few built-in approximations, making them inaccurate even for designing bilayer metastructures. The problem is exacerbated as the number of layers increases because the interactions between different layers

become increasingly complex and thus cannot be captured by the simple unit cell model.

The adjoint optimization technique provides an effective approach for overcoming most of these design limitations. The cost, however, is the significantly increased computational resource requirements, resulting in demonstrations of either very small or 2D devices. The use of parameterized meta-atoms (instead of the conventionally used topological schemes) lays out a way of overcoming the design limitations while decreasing the computation time through reducing the design domain dimensionality. This compromise allows for optimization of 3D structures with volumes as large as a few thousand cubic wavelengths. However, the efficiencies achieved might be lower than what might be possible with a freeform device.

Although the fabrication process of 2.5D metastructures involves more steps than single-layer metasurfaces, the significant performance improvement is large enough to justify the more involved fabrication process. Multilayer structures with tens of nanometer tolerances are routinely fabricated in CMOS foundries, and similar processes can be potentially used to manufacture practical 2.5D multifunctional metastructures such as color-splitting filters for image sensors [47].

**Funding.** Defense Advanced Research Projects Agency; Samsung Advanced Institute of Technology.

See Supplement 1 for supporting content.

<sup>†</sup>These authors contributed equally to this work.

## REFERENCES

1. S. M. Kamali, E. Arbabi, A. Arbabi, and A. Faraon, "A review of dielectric optical metasurfaces for wavefront control," *Nanophotonics* **7**, 1041–1068 (2018).
2. H. T. Chen, A. J. Taylor, and N. Yu, "A review of metasurfaces: physics and applications," *Rep. Prog. Phys.* **79**, 1–59 (2016).
3. N. Yu and F. Capasso, "Flat optics with designer metasurfaces," *Nat. Mater.* **13**, 139–150 (2014).
4. A. Arbabi, E. Arbabi, S. M. Kamali, Y. Horie, S. Han, and A. Faraon, "Miniature optical planar camera based on a wide-angle metasurface doublet corrected for monochromatic aberrations," *Nat. Commun.* **7**, 13682 (2016).
5. W. Zhao, B. Liu, H. Jiang, J. Song, Y. Pei, and Y. Jiang, "Full-color hologram using spatial multiplexing of dielectric metasurface," *Opt. Lett.* **41**, 147–150 (2016).
6. N. Yu, P. Genevet, M. A. Kats, F. Aieta, J.-P. P. Tetienne, F. Capasso, and Z. Gaburro, "Light propagation with phase discontinuities: generalized laws of reflection and refraction," *Science* **334**, 333–337 (2011).
7. A. Arbabi, Y. Horie, M. Bagheri, and A. Faraon, "Dielectric metasurfaces for complete control of phase and polarization with subwavelength spatial resolution and high transmission," *Nat. Nanotechnol.* **10**, 937–943 (2015).
8. A. V. Kildishev, A. Boltasseva, and V. M. Shalaev, "Planar photonics with metasurfaces," *Science* **339**, 1232009 (2013).
9. E. Arbabi, A. Arbabi, S. M. Kamali, Y. Horie, and A. Faraon, "Multiwavelength polarization-insensitive lenses based on dielectric metasurfaces with meta-molecules," *Optica* **3**, 628–633 (2016).
10. C. Pfeiffer and A. Grbic, "Cascaded metasurfaces for complete phase and polarization control," *Appl. Phys. Lett.* **102**, 231116 (2013).
11. P. Lalanne, S. Astilean, P. Chavel, E. Cambriil, and H. Launois, "Blazed binary subwavelength gratings with efficiencies larger than those of conventional échellette gratings," *Opt. Lett.* **23**, 1081–1083 (1998).
12. A. Arbabi, Y. Horie, A. J. Ball, M. Bagheri, and A. Faraon, "Subwavelength-thick lenses with high numerical apertures and large

- efficiency based on high-contrast transmitarrays,” *Nat. Commun.* **6**, 7069 (2015).
13. X. Cheng, T. He, Z. Zhou, J. Zhang, H. Jiao, and Z. Wang, “Multilayer enhanced metasurfaces with high efficiency and additional functionalities,” *Proc. SPIE* **10691**, 1069103 (2018).
  14. J. P. Balthasar Mueller, N. A. Rubin, R. C. Devlin, B. Groever, and F. Capasso, “Metasurface polarization optics: independent phase control of arbitrary orthogonal states of polarization,” *Phys. Rev. Lett.* **118**, 113901 (2017).
  15. M. S. Faraji-Dana, E. Arbabi, A. Arbabi, S. M. Kamali, H. Kwon, and A. Faraon, “Compact folded metasurface spectrometer,” *Nat. Commun.* **9**, 4196 (2018).
  16. A. Arbabi, E. Arbabi, Y. Horie, S. M. Kamali, and A. Faraon, “Planar metasurface retroreflector,” *Nat. Photonics* **11**, 415–420 (2017).
  17. Y. Zhao and A. Alù, “Manipulating light polarization with ultrathin plasmonic metasurfaces,” *Phys. Rev. B* **84**, 205428 (2011).
  18. Y. Zhou, I. I. Kravchenko, H. Wang, J. R. Nolen, G. Gu, and J. Valentine, “Multilayer noninteracting dielectric metasurfaces for multiwavelength metaoptics,” *Nano Lett.* **18**, 7529–7537 (2018).
  19. M. Khorasaninejad, F. Aieta, P. Kanhaiya, M. A. Kats, P. Genevet, D. Rousso, and F. Capasso, “Achromatic metasurface lens at telecommunication wavelengths,” *Nano Lett.* **15**, 5358–5362 (2015).
  20. J. Ding, S. An, B. Zheng, and H. Zhang, “Multiwavelength metasurfaces based on single-layer dual-wavelength meta-atoms: toward complete phase and amplitude modulations at two wavelengths,” *Adv. Opt. Mater.* **5**, 1–8 (2017).
  21. F. Aieta, M. A. Kats, P. Genevet, and F. Capasso, “Multiwavelength achromatic metasurfaces by dispersive phase compensation,” *Science* **347**, 1342–1345 (2015).
  22. E. Arbabi, A. Arbabi, S. M. Kamali, Y. Horie, and A. Faraon, “Multiwavelength metasurfaces through spatial multiplexing,” *Sci. Rep.* **6**, 32803 (2016).
  23. S. M. Kamali, E. Arbabi, A. Arbabi, Y. Horie, M. S. Faraji-Dana, and A. Faraon, “Angle-multiplexed metasurfaces: encoding independent wavefronts in a single metasurface under different illumination angles,” *Phys. Rev. X* **7**, 041056 (2017).
  24. B. Walther, C. Helgert, C. Rockstuhl, F. Setzpfandt, F. Eilenberger, E.-B. Kley, F. Lederer, A. Tünnermann, and T. Pertsch, “Spatial and spectral light shaping with metamaterials,” *Adv. Mater.* **24**, 6300–6304 (2012).
  25. S. Wang, P. C. Wu, V. C. Su, Y. C. Lai, C. Hung Chu, J. W. Chen, S. H. Lu, J. Chen, B. Xu, C. H. Kuan, T. Li, S. Zhu, and D. P. Tsai, “Broadband achromatic optical metasurface devices,” *Nat. Commun.* **8**, 187 (2017).
  26. R. Matzen, J. S. Jensen, and O. Sigmund, “Topology optimization for transient response of photonic crystal structures,” *J. Opt. Soc. Am. B* **27**, 2040–2050 (2010).
  27. J. S. Jensen and O. Sigmund, “Topology optimization for nano-photonics,” *Laser Photon. Rev.* **5**, 308–321 (2011).
  28. A. Y. Piggott, J. Lu, K. G. Lagoudakis, J. Petykiewicz, T. M. Babinec, and J. Vuković, “Inverse design and demonstration of a compact and broadband on-chip wavelength demultiplexer,” *Nat. Photonics* **9**, 374–377 (2015).
  29. S. Molesky, Z. Lin, A. Y. Piggott, W. Jin, J. Vucković, and A. W. Rodriguez, “Inverse design in nanophotonics,” *Nat. Photonics* **12**, 659–670 (2018).
  30. O. D. Miller, *Photonic Design: from Fundamental Solar Cell Physics to Computational Inverse Design* (University of California, Berkeley, 2012).
  31. C. M. Lalau-Keraly, S. Bhargava, O. D. Miller, and E. Yablonovitch, “Adjoint shape optimization applied to electromagnetic design,” *Opt. Express* **21**, 21693–21701 (2013).
  32. A. C. R. Niederberger, D. A. Fattal, N. R. Gauger, S. Fan, and R. G. Beausoleil, “Sensitivity analysis and optimization of sub-wavelength optical gratings using adjoints,” *Opt. Express* **22**, 12971–12981 (2014).
  33. L. Frandsen, A. Harpoth, P. Borel, M. Kristensen, J. Jensen, and O. Sigmund, “Broadband photonic crystal waveguide 60 degrees bend obtained utilizing topology optimization,” *Opt. Express* **12**, 5916–5921 (2004).
  34. A. Iguchi, Y. Tsuji, T. Yasui, and K. Hirayama, “Efficient topology optimization of optical waveguide devices utilizing semi-vectorial finite-difference beam propagation method,” *Opt. Express* **25**, 28210–28222 (2017).
  35. Y. Lefevre, P. Wahl, N. Vermeulen, and H. Thienpont, “Adjoint-enabled optimization of optical devices based on coupled-mode equations,” *Opt. Express* **22**, 19423–19439 (2014).
  36. D. Sell, J. Yang, S. Doshay, R. Yang, and J. A. Fan, “Large-angle, multifunctional metagratings based on freeform multimode geometries,” *Nano Lett.* **17**, 3752–3757 (2017).
  37. M. Mansouree and A. Arbabi, “Large-scale metasurface design using the adjoint sensitivity technique,” in *Conference on Lasers and Electro-Optics (CLEO)* (2018), paper FF1F.7.
  38. M. Mansouree and A. Arbabi, “Metasurface design using level-set and gradient descent optimization techniques,” in *International Applied Computational Electromagnetics Society Symposium* (2019).
  39. Z. Lin, B. Groever, F. Capasso, A. W. Rodriguez, and M. Lončar, “Topology-optimized multilayered metaoptics,” *Phys. Rev. Appl.* **9**, 044030 (2018).
  40. Z. Lin and S. G. Johnson, “Overlapping domains for topology optimization of large-area metasurfaces,” arXiv:1906.05376 (2019).
  41. A. Zhan, T. K. Fryett, S. Colburn, and A. Majumdar, “Inverse design of optical elements based on arrays of dielectric spheres,” *Appl. Opt.* **57**, 1437–1446 (2018).
  42. J. Yang and J. A. Fan, “Topology-optimized metasurfaces: impact of initial geometric layout,” *Opt. Lett.* **42**, 3161–3164 (2017).
  43. V. Liu and S. Fan, “S4: A free electromagnetic solver for layered periodic structures,” *Comput. Phys. Commun.* **183**, 2233–2244 (2012).
  44. A. F. Oskooi, D. Roundy, M. Ibanescu, P. Bermel, J. D. Joannopoulos, and S. G. Johnson, “MEEP: a flexible free-software package for electromagnetic simulations by the FDTD method,” *Comput. Phys. Commun.* **181**, 687–702 (2010).
  45. M. Mansouree and A. Arbabi, “Multi-layer multifunctional metasurface design using the adjoint sensitivity technique,” *Proc. SPIE* **10928**, 109281N (2019).
  46. H. Chung and O. D. Miller, “High-NA achromatic metalenses by inverse design,” arXiv:1905.09213 (2019).